A polymer/semiconductor write-once read-many-times memory

Sven Möller[1], Craig Perlov[2], Warren Jackson[2], Carl Taussig[2] & Stephen R. Forrest[1]

[1]*Department of Electrical Engineering and Center for Photonics and Optoelectronic Materials, Princeton University, Princeton, New Jersey 08544, USA*
[2]*Hewlett-Packard Laboratories, Palo Alto, California 94304, USA*

Organic devices promise to revolutionize the extent of, and access to, electronics by providing extremely inexpensive, lightweight and capable ubiquitous components that are printed onto plastic, glass or metal foils[1–3]. One key component of an electronic circuit that has thus far received surprisingly little attention is an organic electronic memory. Here we report an architecture for a write-once read-many-times (WORM) memory, based on the hybrid integration of an electrochromic polymer with a thin-film silicon diode deposited onto a flexible metal foil substrate. WORM memories are desirable for ultralow-cost permanent storage of digital images, eliminating the need for slow, bulky and expensive mechanical drives used in conventional magnetic and optical memories. Our results indicate that the hybrid organic/inorganic memory device is a reliable means for achieving rapid, large-scale archival data storage. The WORM memory pixel exploits a mechanism of current-controlled, thermally activated un-doping of a two-component electrochromic conducting polymer.

Ultralow-cost WORM memories have widespread uses in varied applications, such as the rapid, archival storage of video images (that is, they are similar to 'flash' memories except that the data storage is permanent)[4–7], where the vulnerability to breakage and the relatively high cost associated with slow and power-hungry magnetic or optical disk drives are not acceptable. In a two-dimensional WORM memory array, the memory 'pixels' are read row-by-row. This architecture requires a nonlinear electronic element, such as a p–n junction diode, at each intersection of the row and column electrodes (Fig. 1, top). Furthermore, to distinguish between a 'written' pixel (for example, one that contains a logical '1') from an unwritten pixel (logical '0'), it is necessary to integrate a writable fuse in series with the diode. The fuse can be normally closed, or normally open (that is, an 'anti-fuse'), with the former device more suitable for testing and quality assurance of the unwritten memory. The fuse must be capable of reliable and rapid opening on the application of current or voltage of a significantly different magnitude than that used to read the memory, and it must have long-term operational stability in both the written and the unwritten states. Here we demonstrate a fused memory pixel consisting of the conductive electrochromic polymer (Baytron P, from Bayer Corp.)[8,9], polyethylenedioxythiophene (PEDT):polystyrene sulphonic acid (PSS) (or 'PEDOT'), layered onto the surface of a thin-film Si p–i–n diode deposited onto a stainless steel substrate (Fig. 1, bottom).

The fused switching of the memory element (see Methods section for fabrication details) is shown in Fig. 2. The forward current of the Si diode (open circles) reaches 100 μA at a voltage of 1.5 V, whereas under reverse bias, the leakage is only 2.3 nA at −1.5 V, giving a rectifying ratio of $\sim 10^5$. Owing to the series resistance of the polymer film (of thickness $d = 40$ nm), the forward current is reduced to 400 nA for the hybrid device. Furthermore, the reverse leakage current is also increased (leading to a rectification ratio of ~50, see Fig. 2), owing to the presence of a large-area, conducting polymer layered across the full Si surface. In a passive matrix memory, the Si and polymer regions between the row and column contacts are selectively removed, thus eliminating this shunt path. Indeed, removing the 50-nm-thick PEDOT layer in a fused Si device by exposure to an oxygen plasma reduced the dark current by a factor of more than 3×10^3.

To switch the fuse state from 'closed' to 'open', the voltage is ramped at 1.0 V s^{-1} from 0 V → 10 V → 0 V. During each voltage step of duration $t_d = 10$ ms, the voltage is applied for $\tau = 4$ ms (a 40% duty cycle) (Fig. 3a inset). On applying this cyclic voltage ramp, the fuse opens, reducing the current to a background leakage of ≤10 pA at all voltages applied. Hence, the contrast between a '1' and '0' increases by $\sim 10^4$ at a forward bias of 1.5 V. In switching ~200 PEDOT films, the film always made the transition to the non-conducting state without a single short observed. The reliability,

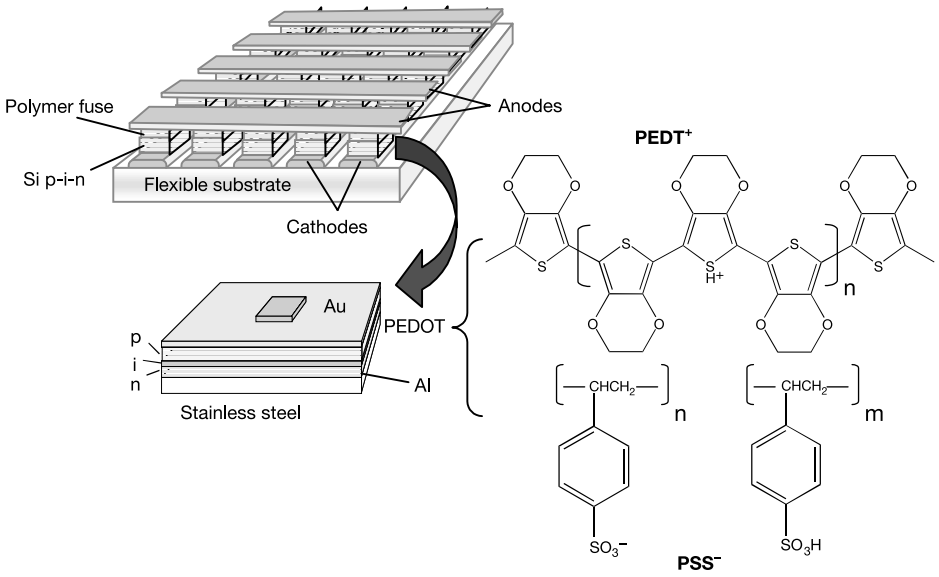

Figure 1 Generalized architecture of the WORM memory, and the materials used in its implementation. Top, conceptual view of a hybrid organic/inorganic semiconductor WORM memory. Bottom, diagram of the WORM memory element used in this study, employing an Al cathode coated, flexible stainless steel substrate. Also shown is the chemical structural formula of the two-component conductive electrochromic polymer, PEDOT, used as the fuse material in the WORM memory element. See text for details.

irreversibility and reproducibility of the switching process are essential to a practical memory array.

To clarify the origin of the switching process, we show in Fig. 3a the current density (J) as a function of voltage (V) for a $d = 40$ nm film sandwiched between ITO (indium tin oxide) and Au contacts, where $\tau = 4$ ms, while the voltage is swept as before. The film undergoes a transition to its high-resistivity state by traversing two distinct regions: region A, from $V = 0$ to 4 V, and region B at $V \geq 4$ V. Despite the apparent complexity of the switching process, films of all thicknesses and under all bias regimes investigated qualitatively exhibit the same features in their J–V characteristics.

At the lowest voltages (0–2 V), the current density is reversible over the timescale of the experiment (minutes). At higher voltages, the current reaches a first peak, followed by a second peak, as shown in detail in Fig. 3b. The permanent conductivity changes induced by sweeps of up to 4 V are small (~3–5 times lower than the unstressed film), and their magnitude depends on the pulse length, τ, as shown in Fig. 3b. The second, sharp peak appears at lower voltages, is reduced in magnitude, and broadens as τ is increased from 0.5 ms to 4 ms. However, once the film is biased into region B, a qualitatively different process is initiated, resulting in a dramatic and permanent decrease in conductivity. Indeed, once the last broad peak appears, J decreases precipitously, corresponding to a reduction in conductivity by several orders of magnitude. Hence, on the return sweep, the fuse is opened.

Figure 4a shows the transient response of a 55-nm-thick PEDOT film sandwiched between Au and ITO electrodes at several different voltages. At >5 V, there are two clearly resolved regions: a first plateau (open arrow), followed by a current peak (filled arrow). The delay between the pulse onset and the peak decreases with increasing voltage, reaching a current density of 700 A cm^{-2} after only 1 μs for a pulse height of 12 V. As in the voltage sweeps in Fig. 3, the current peak corresponds to the initiation of a permanent change in film conductivity, leading to the very-high-resistance phase of the open fuse. Switching times of ~2 μs are observed in the thinnest ($d = 25$ nm) PEDOT films.

The peak delay from the voltage-pulse leading edge is linearly dependent on $1/(V - V_{offset})$, where $V_{offset} = 4.5$ V is the voltage drop across the Au contact necessary to inject an appreciable concentration of electrons. The transient response can be understood in terms of the double carrier injection previously observed in amorphous Si p–i–n diodes[10]. In PEDOT, the current is primarily carried by holes[11]. However, at $V > V_{offset}$, electrons are injected, thereby neutralizing some of the hole space charge current. This, in turn, increases the internal electric field within the polymer, leading to a further increase in hole current. Under these conditions, the hole current exceeds that in the absence of the counter electron charge by the 'double injection gain', giving rise to a current peak. At the higher pulse voltages, the peak delay decreases owing to the larger density of injected electrons. Although the current is controlled by the presence of electrons, the electrons themselves do not contribute appreciably to the current in Fig. 4a. The peak delay follows $t = d^2/\mu_n(V - V_{offset})$ as shown in Fig. 4b, leading to an electron mobility of $\mu_n = (1.7 \pm 0.4) \times 10^{-6}$ cm^2 V^{-1} s^{-1}, much lower than the hole mobility of ~0.1 cm^2 V^{-1} s^{-1} for this predominately hole-transporting polymer.

Energy-barrier lowering via electron injection also suggests the origin of the permanent conductivity changes. As PSS is electrically insulating, conduction occurs by hole transport along low-resistivity percolation pathways formed by PEDT$^+$ chains throughout the film. The energy levels of PEDT$^+$ responsible for charge transport[8,12,13] are shown in Fig. 4b, top inset. Holes can readily be injected from both Au and ITO into the highest occupied molecular orbital (HOMO) of PEDT$^+$ at 5.0 eV. Although the lowest unoccupied molecular orbital (LUMO) is only 0.6 eV above the HOMO, there is nevertheless a large energy barrier to overcome for electron injection. To promote injection of an electron, PEDT$^+$ is electrochemically reduced to PEDT^0, and the energy level scheme changes

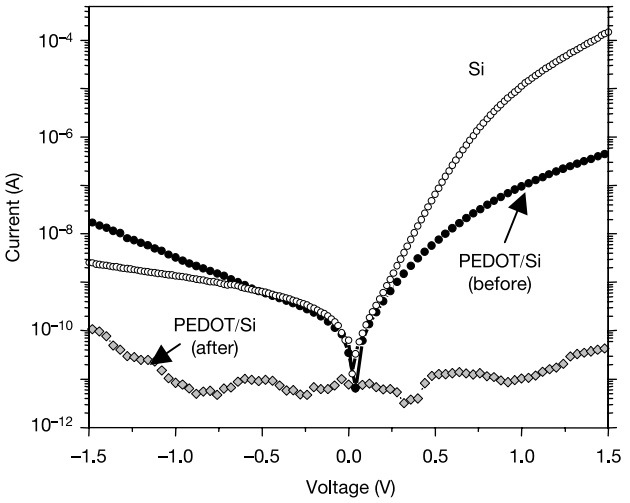

Figure 2 The switching characteristics of the WORM memory pixel. Open circles, the current/voltage characteristics of an as-deposited thin-film Si p–i–n diode; filled circles, data for an integrated 40-nm-thick PEDOT fuse /thin-film Si p–i–n diode WORM memory device in the unwritten state; diamonds, data for the WORM device in the written (blown fuse) state.

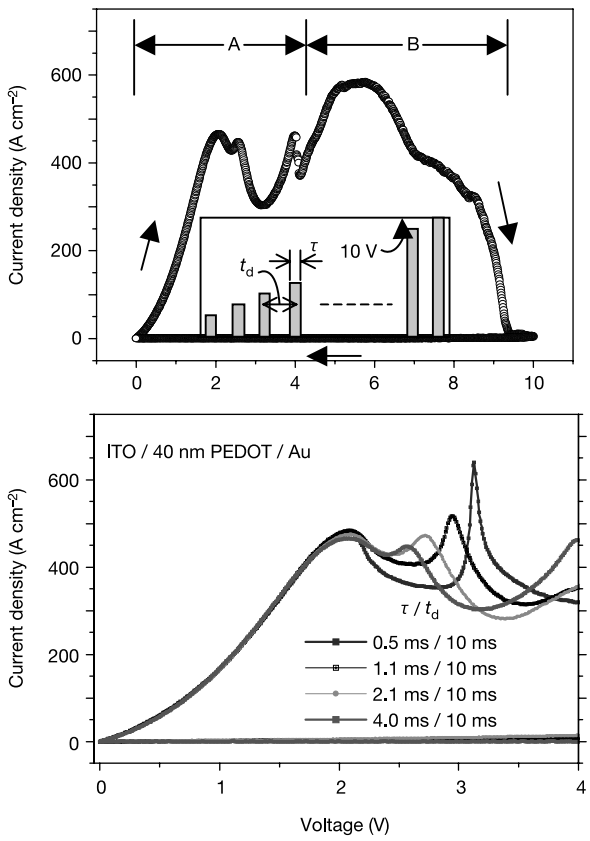

Figure 3 The switching process of the WORM memory pixel is shown under several different writing conditions. **a**, Quasi-static current density versus voltage characteristics of a 40-nm-thick PEDOT film using a pulse delay of $t_d = 10$ ms and a pulse duration of $\tau = 4$ ms. Note regions A and B. Inset, film switching sequence, defining the switching times used in the figure. **b**, Detail of the switching process occurring in region A using different τ ranging from 0.5 to 4 ms.

to that in Fig. 4b, bottom inset. In the neutral state, $PEDT^0$, electrons can only occupy the LUMO at 3.9 eV, and the optical energy gap increases to 1.5 eV. Hence, there is rapid sequential oxidation and reduction by the successive transfer of holes and electrons into the polymer.

As voltage is increased beyond the first peak in region A, the sample temperature increases, leading to enhanced oxidation of $PEDT^0$ accompanied by a decrease in film conductivity due to lower charge carrier concentration and/or hole mobility along the polymeric backbones. The second peak in region A shows a similar behaviour, suggesting the presence of a second species of chains with a slightly different reduction potential or chain environment within the film. Although PEDOT films are morphologically smooth, the aqueous dispersion contains particles of different sizes consisting of interpenetrating coils of PEDT and PSS chains. The shift of the peak towards lower voltage with increasing τ is then due to slow diffusion of electrons branching into these morphologically distinct domains.

The reduction of $PEDT^+$ continues with increasing current until a maximum number of chains in the neutral $PEDT^0$ state are achieved for all τ, and the process saturates at voltages >2 V but still within region A. At yet higher voltages above $V_{offset} \approx 4.5$ V, electron injection leads to the process that characterizes region B—a large, permanent decrease in film conductivity by up to a factor of 10^3. The magnitude and rapidity of the change to the low-conductivity state depends on τ and duty cycle, indicating that thermal effects contribute at high current densities. Permanent conductivity changes by thermal undoping of the polymer at elevated temperatures have been previously reported[14]. Calculations of the temperature rise during the current transients, based on the heat capacity and thermal conductivities typical of polymers, suggests that the maximum temperatures of ~200 °C required to initiate the undoping process[14] are reached at current densities of ~1 kA cm^{-2} within the first 1 μs of the voltage pulse.

An $N \times N$ pixel matrix memory is addressed row-by-row by measuring the current flowing from N columns to the row in question. Hence, the maximum number of pixels in a row that can be accommodated without leading to read errors (that is, detecting that a pixel is written when in fact it has not been) is $N = \mathrm{mod}|I_{F1}/I_{F0}|/S_B \approx 10^3$, assuming that the signal-to-background current ratio required to reliably distinguish a '1' from a '0' is $S_B = 10$. Here, I_{F1} and I_{F0} are the forward biased currents for the two logical states. On the basis of the performance of our devices, a 1 megabit (1 Mbit) WORM memory is therefore feasible, assuming that the current of a written pixel is $<10^{-4}$ times that of the forward-biased current of a single element in the 1 Mbit memory. Then the sum of the leakage currents from non-addressed diodes in a particular row does not significantly affect I_{F1}/I_{F0}; this condition is met for the devices in Fig. 2.

Such a memory block could be written within 1 s, and would occupy approximately 1 mm^2, assuming that each pixel is 500 nm on a side, with a 50% filling of the array with memory elements. The concept is therefore adaptable to very large (up to 100 Mbit, depending on the addressing and writing schemes used) two-dimensional arrays that can be both read and written on short timescales (<1 s, using interleaved row scanning), consistent with the highest-performance archival WORM memories.

Finally, it is worth considering the advantages of the WORM over other, existing memory technologies. For example, erasable programmable read-only memory (EPROM) and flash memories rely on three-terminal crystalline Si transistor memory cells patterned using photolithography, whereas our device consists simply of a cross point with no critical alignments, deposited onto a thin film of non-crystalline Si on a foil substrate. Further, three-terminal memory cells occupy an area of $9F^2$, where F is the minimum feature size, while the cell for the WORM occupies only $4F^2$ (where $F \approx 500$ nm). Moreover, because of the higher temperatures and crystalline materials required for conventional memories, these platforms cannot be easily stacked to form a high-density three-dimensional memory—a non-existent limitation for the WORM memory. Thus, the non-crystalline organic cross point memory can exceed the potential density of these alternative, established memories in all three dimensions at lower cost. □

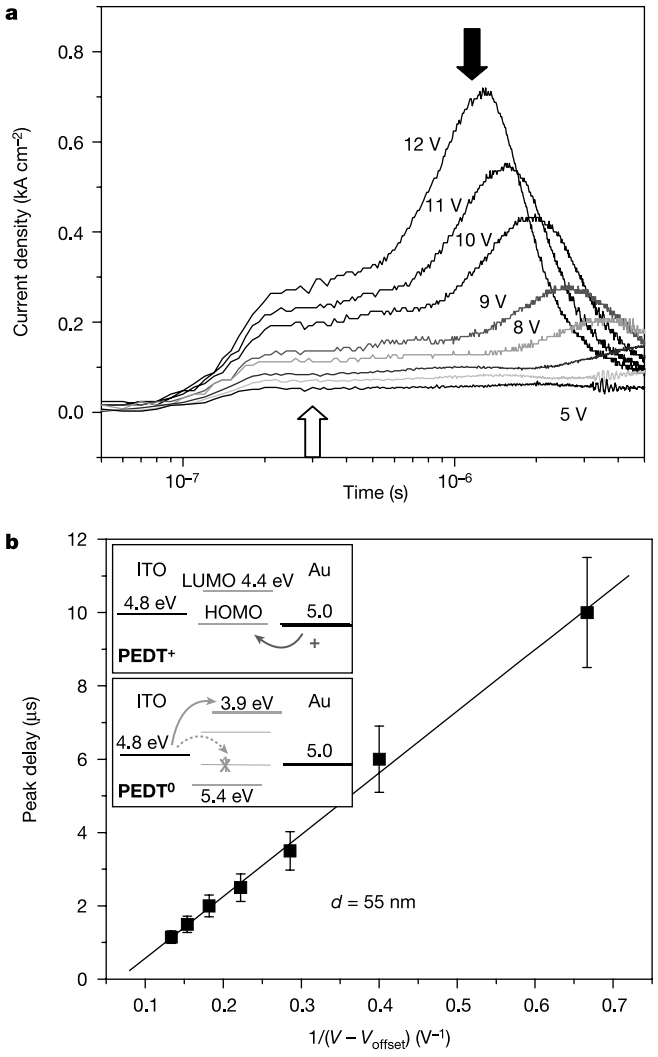

Figure 4 The behaviour of the WORM memory element under transient voltage pulse conditions. **a**, Transient response of the current density across a 60-nm-thick PEDOT film as a function of applied voltage during the pulse. The pulse duration is >10 μs, obtained using a voltage pulse generator with a rise time of 100 ns, limiting the current transient response observed at the onset of the pulse. Open arrow shows the plateau region where no changes in conductivity are observed; the filled arrow indicates the current peak corresponding to the process where there is a significant drop in conductivity, as is apparent from the slow drop in current density following the peak. **b**, Peak transient delay as a function of $1/(V - V_{offset})$, where $V_{offset} = 4.5$ V is required for electron injection across the Au/PEDOT barrier. The straight-line fit to the data yields an electron mobility of $\mu_n = (1.7 \pm 0.4) \times 10^{-6}$ cm^2 V^{-1} s^{-1}. Inset, the energy level diagrams of PEDT in the oxidized (upper panel) and neutral (lower panel) states, along with the electrode arrangement in the films used in Figs 3 and 4.

Methods

The memory element comprises a thin-film silicon p–i–n diode and thin layer of PEDOT deposited onto the p-Si contact surface by spinning the aqueous dispersion at a rate of between 2,000 r.p.m. (resulting in a film thickness of $d = 60$ nm) and 6,000 r.p.m. (yielding $d = 25$ nm). To remove residual water, the films were baked at 140 °C for 1 h in a nitrogen-filled glove box (<1 p.p.m. O_2, <1 p.p.m. H_2O). High-conductivity Baytron P AI4071 was used, with a solid content of ~1.5% and a PEDT:PSS weight ratio of 1:2.5. In the p-doped

state, PEDOT films exhibit conductivities of up to 1 S cm^{-1}, with a principal absorption edge at 0.6 eV, making it optically absorbing in the infrared but transparent across the visible spectrum[8,9]. The thin-film Si diodes were fabricated by low-temperature deposition on a lightweight, stainless steel substrate coated with a 100-nm-thick Al layer that served as the cathode. The p–i–n rectifying structures consisted of a grown, 15-nm n$^+$Si/400-nm undoped (intrinsic) i-Si/25-nm p$^+$Si junction region. To independently investigate the switching properties of the polymer, an ITO/polymer/metal sandwich device was fabricated on precleaned, 20 Ω per square, ITO-coated glass substrates. All devices are contacted on the polymer surface via thermally evaporated, 17 μm^2 Au electrodes. The devices were electrically characterized in air. In our temperature simulations, the thermal impedance between the film and substrate is neglected. This implies that within the first ~100 ns of the voltage onset, the substrate/film interface remains at room temperature.

Received 15 April; accepted 12 September 2003; doi:10.1038/nature02070.

1. Forrest, S. R., Burrows, P. E. & Thompson, M. E. Organic emitters promise a new generation of displays. *Laser Focus World*, Feb., 99–101 (1995).
2. Gelinck, G. H., Geuns, T. C. T. & Leeuw, D. M. d. High-performance all-polymer integrated circuits. *Appl. Phys. Lett.* **77,** 1487–1489 (2000).
3. Peumans, P., Yakimov, A. & Forrest, S. R. Small molecular weight organic thin-film photodetectors and solar cells. *J. Appl. Phys.* **93,** 3693–3723 (2003).
4. Saluel, D., Daval, J., Bechevet, B., Germain, C. & Valon, B. Ultra high density data storage on phase change materials with electrical micro-tips. *J. Magn. Magn. Mater.* **193,** 488–491 (1999).
5. Asokan, S. Electrical switching in chalcogenide glasses—Some newer insights. *J. Optoelectron. Adv. Mater.* **3,** 753–756 (2001).
6. Stocker, H. J. Bulk and thin film switching and memory effects in semiconducting chalcogenide glasses. *Appl. Phys. Lett.* **15,** 55–57 (1969).
7. Hua, Z. Y., Chen, G. R., Xu, W. & Chen, D. Y. New organic bistable films for ultrafast electric memories. *Appl. Surf. Sci.* **169,** 447–451 (2001).
8. Heuer, H. W., Wehrmann, R. & Kirchmeyer, S. Electrochromic window based on conducting poly (3,4-ethylenedioxythiophene)poly(styrene sulfonate). *Adv. Funct. Mater.* **12,** 89–94 (2002).
9. Groenendaal, B. L., Jonas, F., Freitag, D., Pielartzik, H. & Reynolds, J. R. Poly(3,4-ethylenedioxythiophene) and its derivatives: Past, present, and future. *Adv. Mater.* **12,** 481–494 (2000).
10. Hack, M. & Street, R. A. Analysis of double injection in amorphous silicon p-i-n diodes. *J. Appl. Phys.* **72,** 2331–2339 (1992).
11. Johansson, T., Pettersson, L. A. A. & Inganas, O. Conductivity of de-doped poly(3,4-ethylenedioxythiophene). *Synth. Met.* **129,** 269–274 (2002).
12. Greczynski, G. *et al.* Photoelectron spectroscopy of thin films of PEDOT-PSS conjugated polymer blend: a mini-review and some new results. *J. Electron Spectrosc. Rel. Phenom.* **121,** 1–17 (2001).
13. Xing, K. Z., Fahlman, M., Chen, X. W., Inganas, O. & Salaneck, W. R. The electronic structure of poly(3,4-ethylene-dioxythiophene): Studied by XPS and UPS. *Synth. Met.* **89,** 161–165 (1997).
14. Pei, Q. B., Zuccarello, G., Ahlskog, M. & Inganas, O. Electrochromic and highly stable poly(3,4-ethylenedioxythiophene) switches between opaque blue-black and transparent sky blue. *Polymer* **35,** 1347–1351 (1994).

Acknowledgements We thank A. Elschner and H. C. Starck for samples of Baytron P, and M. Thompson for discussions. We also thank National Renewable Energy Laboratories for supplying the thin-film Si diodes. This work was supported by HP and the National Science Foundation.

Competing interests statement The authors declare that they have no competing financial interests.

Correspondence and requests for materials should be addressed to S.R.F. (forrest@princeton.edu).

Rapid body size decline in Alaskan Pleistocene horses before extinction

R. Dale Guthrie

Institute of Arctic Biology, University of Alaska, Fairbanks, Alaska 99775, USA

About 70% of North American large mammal species were lost at the end of the Pleistocene epoch[1]. The causes of this extinction—the role of humans versus that of climate—have been the focus of much controversy[1–6]. Horses have figured centrally in that debate, because equid species dominated North American late Pleistocene faunas in terms of abundance, geographical distribution, and species variety, yet none survived into the Holocene epoch. The timing of these equid regional extinctions and accompanying evolutionary changes are poorly known. In an attempt to document better the decline and demise of two Alaskan Pleistocene equids, I selected a large number of fossils from the latest Pleistocene for radiocarbon dating. Here I show that horses underwent a rapid decline in body size before extinction, and I propose that the size decline and subsequent regional extinction at 12,500 radiocarbon years before present are best attributed to a coincident climatic/vegetational shift. The present data do not support human overkill[1] and several other proposed extinction causes[2,3], and also show that large mammal species responded somewhat individualistically to climate changes[4–6] at the end of the Pleistocene.

Caballoid horses in Alaska were probably part of the diverse Eurasian species complex of the stocky *Equus ferus*, judging from their fossil anatomy[7,8] and preserved mitochondrial DNA[9]. In contrast, fossils of the other equid Alaskan species have unusually long gracile metapodials, making them similar to the living *Equus hemionus* from central Asia, and also similar to fossil New World hemione-like forms. So little work has been done with these northern hemione-like equid fossils that I shall call these hemionids for simplicity, but note that their specific relationships remain uncertain.

Alaskan hemionid fossils had not previously been radiocarbon dated. They are comparatively rare in museum collections. In this study, 19 such fossils were dated, and the fact that none of the hemionid metacarpals dated after 31,000 radiocarbon years before present (31 kyr BP) makes their extinction before the Last Glacial Maximum (LGM) seem likely. It is possible that the disappearance of this small-bodied hemionid species somehow affected selection pressures on later Alaskan caballoid horses, promoting reductions in body size and increased numbers of the latter during the LGM, around 18–20 kyr BP, but at present this seems unlikely given the implied time lag between the hemionid extinction and caballoid response.

Compared with the hemionids, caballoid horse fossils from Alaska are much more numerous and much better studied. Previous dates on over 220 fossil specimens from Alaska and the Yukon Territory[10,11] revealed no dates later than 12.5 kyr BP. Other studies from Eurasia and Beringia had indicated a size decline among horses at some time during the late Pleistocene[12,13], but the exact timing was uncertain. Unlike previous studies, I chose to date metacarpals exclusively in order to better assess any subtle changes in body size with time and how this related to extinction. The dramatic size changes recorded just before extinction were most unexpected (Fig. 1). Explanations for these apparent size changes include the possibility that my sampling methods may somehow have affected this plot and artificially created a drop in apparent metacarpal size. This seems unlikely (see Methods). I suspect that the gap in dates at 28–35 kyr BP may reflect lower population numbers during this time, because previous, non-metacarpal, radiocarbon work on Alaskan horse fossils also showed comparatively few dates during this pre-LGM period[14].

A second possibility is that a new species or morphotype of smaller horses immigrated into Alaska, creating the illusion of size decline. The apparent high metacarpal variability during the LGM (Fig. 1) as opposed to post-LGM suggests such an interpretation. Some of this variability may simply be due to the greater abundance of LGM dates. In addition, species in transition from one adaptive peak to another, undergoing rapid evolution, are often more variable[15]. The graph of size/time does not show two overlapping clusters, as one would expect with species replacement. Instead, smaller variants continue to emerge on the graph over time, and larger variants continue to fall out. This would necessitate multiple species replacements. In contrast, the explanation of a simple body-size decline in one widespread population seems much more parsimonious. Comparable size declines at the end of the Pleistocene are not unique to horses[16]. Bison declined more dramatically in an even shorter time span[17] but at a later date.

The significance of this size decline among Alaskan horses just before their regional extinction is that environmental pressures provoking smaller body size may well have been the same ones that

